FCM_{PASS} Software Aids Extracellular Vesicle Light Scatter Standardisation

Joshua A. Welsh[1,2*], Peter Horak[3], James S. Wilkinson [3], Verity J Ford[1], Jennifer C. Jones[2], David Smith[1,4], Judith A. Holloway[1], Nicola A. Englyst[1],

[1]Faculty of Medicine, University of Southampton, UK

[2]Translational Nanobiology Section, Laboratory of Pathology, National Cancer Institute, National Institutes of Health, Bethesda, USA

[3]Optoelectronics Research Centre, University of Southampton, UK

[4]Anaesthetics Department, University Hospital Southampton, UK.

*joshua.welsh@nih.gov corresponding author.

Acknowledgements

The authors would like to thank Michael Ward, PhD and Wesley Smith from ThermoFisher Scientific and Edwin van der Pol, PhD from Amsterdam Medical Centre for useful discussions. We would also like to thank John P. Nolan, PhD for constructive criticism of the manuscript.

Funding

JAW is an International Society for Advancement of Cytometry (ISAC) Marylou Ingram Scholar 2019-2023. This work was supported by University of Southampton, Faculty of Medicine, Doctoral Training Award scheme, Higher Education Innovation Fund, European Association of Cardiothoracic Anaesthesiology, the U.S. National Institutes of Health, National Cancer Institute, 1ZIA-BC011502, and the Intramural Research Program of the National Institutes of Health (NIH), National Cancer Institute, and Center for Cancer Research

Conflict of Interest

JCJ and JAW are inventors on patents and patent applications related to extracellular vesicle analysis. NCI holds a collaborative research and development agreement (CRADA) with Beckman Coulter.

Abstract

The study of extracellular vesicles (EVs) is a rapidly growing field due to their great potential in many areas of clinical medicine including diagnostics, prognostics, theranostics, and therapeutics. Flow cytometry is currently one of the most popular methods of analysing EVs due to it being a high-throughput, multi-parametric technique, that is readily available in the majority of research labs. Despite its wide use, few commercial flow cytometers are designed specifically for the detection of EVs. Many flow cytometers used for EV analysis are working at their detection limits and are unable to detect the majority of EVs. Currently, very little standardisation exists for EV flow cytometry which is an issue because flow cytometers vary considerably in the way they collect scattered or fluorescent light from particles being interrogated. This makes published research hard to interpret, compare, and in some cases, impossible to reproduce. Here we demonstrate a method of flow cytometer light scatter standardisation, utilising flow cytometer post-acquisition analysis software (FCM_{PASS}). FCM_{PASS} is built upon Mie theory and enables the approximation of flow cytometer geometric parameters either by analyzing beads of known diameter and refractive index or by inputting the collection angle if known. The software is then able to create a scatter-diameter curve and scatter-refractive index curve that enables researchers to convert scattering data and instrument sensitivity into standardised units. Furthermore, with the correct controls, light scatter data can be converted to diameter distributions or refractive index distributions. FCM_{PASS} therefore offers a freely available and ergonomic method of standardizing and further extending EV characterization using flow cytometry.

Keywords: extracellular vesicles, flow cytometry, standardization, light scatter, Mie modelling, software

Introduction

Extracellular vesicles (EVs) which include exosomes (30-150 nm) and microvesicles (30-1000 nm) are shed by cells, with other types also known to exist [1]. These small vesicles have a phospholipid bilayer containing proteins and an inner cytosolic portion that contains cargo including proteins, metabolites and/or genetic content [2, 3]. Research utilising EVs is growing due to their diagnostic and therapeutic potential, with many laboratories opting to use flow cytometry for their detection [4]. The full size range of EVs cannot be detected in the majority of conventional flow cytometers which are developed to characterise cells.

Early literature using light scatter signals to gate EV populations employed reference particles such as polystyrene beads and, more recently, silica beads. For example, polystyrene reference beads of ~1 μm diameter have been used as reference particles for the larger diameter microvesicles [5, 6, 7, 8]. Polystyrene beads are also commonly used today by manufacturers to demonstrate flow cytometer scatter sensitivity. Using polystyrene or silica reference beads for EV sizing results in a systematic error in EV diameter estimation, as the refractive indices of these beads differ significantly from that of EVs in their light scatter properties [9]. A solution to this problem is converting the scatter parameter in arbitrary units to a standardised unit that would allow comparisons across cytometers. Developing a standardised unit for flow cytometer scatter is, however, non-trivial and must begin with basic models of Mie scattering and some basic concepts.

Light scatter is the process whereby light hits a particle and then changes direction, this includes reflection and refraction. In the context of flow cytometry, a laser beam is focused upon a stream in which particles are suspended. When a particle traverses through the laser beam, light is scattered in all directions by the illuminated particle. In conventional flow cytometry, light scatter is collected perpendicular to the illumination source, known as the parameter, side scatter (SSC), and in the same direction as the illumination source, known as the parameter, forward scatter (FSC). The amount of light scatter by a particle however is dependent on a large number of factors.

To quantify the amount of light reaching a detector in absolute units, the collection geometry of the system from the particle to the detector must be known as this limits the photons that can reach the detector. The geometry that has the largest effect on the number of photons reach the detector

is the flow cell. Flow cells tend to be made of quartz and have inner and outer dimensions, both of which tend to be rectangles – though square flow cells are also used. The range of angles that can be collected by the SSC detector is most often limited by either the inner or the outer flow cell dimensions. Once the collection angle is known, calculating the collected light scatter from a particle can be carried out as there is now a range of angles to integrate the angular scattering distribution of the particle over.

Popular methodologies for determining the amount of light scattered from small particles are Mie scattering and Rayleigh scattering. Rayleigh scattering theory is the simpler methodology of the two, but only applies to predicting light scatter from particles whose diameter is less than one tenth of the incident wavelength. Mie scattering theory was first published in 1908 by Gustav Mie and is built upon the Maxwell equations, and provides a means to calculate the angular light scattering distribution of spherical particles of any diameter, and has successfully been applied to flow cytometry [9, 10]. Furthermore, core-shell structures (**Figure 1B**) such as EVs, which comprise of a cytosolic core and a membrane shell, can be readily modelled using Mie scattering. Mie scattering theory is therefore well-suited to modelling the scattering distribution of the full range of EVs as well as homogeneous spheres (**Figure 1C**) of polystyrene and silica reference beads.

While mathematically it is possible to predict the power of collected light scatter from a particle, collected within a certain geometry, there are several variables to account for which are hard to measure, including: the transmission efficiency of light from the particle to the detector, the laser intensity, and detector variables such as quantum efficiency, as well as user defined detector variable such as gain and voltage. Normalising flow cytometry light scatter data from arbitrary units to standard units of scattering in power is therefore difficult. We believe the most practical unit to normalise the arbitrary scattering measurements to is the scattering cross-section; this is obtained by integrating the differential scattering cross section over the angles collected by the detector within the flow cytometer. The scattering cross section is a hypothetical area describing the probability of light, with unit incident irradiance, being scattered by a particle. The power of scattered light is directly proportional to this cross section and to the incident laser power. The calculation of integrated scattering cross section, however, requires fewer instrument variables to be measured for its calculation. For small particles, the scattering cross-sections is best denoted in units of nm^2. From here on in we refer to the scattering cross-section as the collected light integrated over the collection range of the system.

In this paper, we give an illustration of the interdependence of collection angle, diameter, and RI using Mie theory. We then go on to demonstrate the ability of the FCM_{PASS} software to (i) experimentally estimate the half-angle of the collection cone for three commercial flow cytometers, (ii) we show that approximating the cytometer collection angle can lead to accurate sizing of a range of NIST-traceable beads in various instruments and (iii) we can apply standardised units to flow cytometry SSC data.

Methods

Modelling of light scattering by nanoparticles

To predict the angular light scattering behaviour of particles, a numerical model for scattering from coated and homogeneous spheres from a linearly polarized incident plane wave was implemented in MATLAB (v. 9.0.0.341360, Mathworks, USA), based on Mie theory, using the scripts by C. Maetzler[11]. The scattering cross sections plotted are based on the sum of intensities of the two orthogonal components, ${S_1}^2$ and ${S_2}^2$. Further details of the calculation can be found in **Supplementary Material 1**. The coated spheres modelled are based on the membrane and cytosol of EVs with refractive indices taken from the literature [12, 13, 14, 15, 16, 17], while the homogenous spheres modelled are based on the reference particles with refractive indices given by the Sellmeier equations [18] for silica:

$$n^2 - 1 = \frac{0.6961663\lambda^2}{0.0684043^2} + \frac{0.4079426^2}{\lambda^2 - 0.1162414^2} + \frac{0.897494\lambda^2}{\lambda^2 - 9.896161^2}$$

and polystyrene:

$$n^2 - 1 = \frac{1.4435\lambda^2}{\lambda^2 - 0.020216}.$$

The particle diameters modelled ranged from 1 to 3000 nm to cover both EVs and reference particles [9]. Angular scattering distributions for θ were determined in 1° increments from 0-180° in relation to the incident beam, for each modelled particle. Models showing the angular scattering distribution were not integrated over ϕ. Scattering cross section for flow cytometer models were calculated by using flow cytometer collection angles as an integral over the differential scattering cross section. The collection angles assumed symmetrical collection at 90° to the incident laser beam, in order to model the collection of side-scattered light through a finite aperture. See **Figure 1A** for a schematic of the geometry, see **Supplementary Methods** for further details on Mie calculations

Analysis of beads by flow cytometry

NIST-traceable beads, **Table 1**, were serially diluted in Dulbecco's phosphate-buffered saline (DPBS) until a concentration minimising coincidence detection with a stable fluorescent intensity was determined. Beads were analysed at the lowest flow rate obtainable on each instrument and a minimum of 5,000 events were recorded. Flow cytometer voltages were adjusted so that beads with the maximum and minimum scattering were within the dynamic range of the side scattering collection (SSC) detector. Thresholds were set on SSC on all instruments and were placed so that they were below the 203 nm and 490 nm bead populations. Instruments used were LSR Fortessa, FACS Canto I, and Special Order LSR Fortessa X-20 (all by Becton Dickinson, Oxford, UK). All flow cytometers used an optical bandpass filter centered at 488 nm wavelength with a bandwidth of 10 nm (488/10 filter).

Flow cytometer calibration with reference particles and particle diameter estimation

Acquired bead data from each cytometer was input into post-analysis software, FlowJo v10.1 (FlowJo LLC, Ashland, USA). Each bead population was gated individually with the SSC statistics calculated for each. This SSC statistics for each population were then inputted into a MATLAB script that also contained the bead population mean diameter and refractive index from the manufacturer's technical specifications, **Table 1**.

Once the instrument SSC collection angle was determined (either by considering the imaging optics or by fitting the simulations to the measured data, see Results section), this angle was then used to create predicted data for the beads, creating a curve for each unique bead refractive index. Recorded SSC values from each of the machines were normalised to their predicted data with a single normalisation factor, in order to relate the arbitrary flow cytometer channel count units to the particle scattering cross section in absolute units of nm^2 as calculated by the MATLAB scripts using Mie theory. This single normalisation factor was obtained as the mean of the normalisation factors of each bead population, calculated by dividing the measured SSC value by the predicted value for each population. These scripts were compiled into the publicly available 'FCM_{PASS}', available at http://www.joshuawelsh.co.uk/fcmpass/. **Supplementary Table 1** shows the development of the software.

Biological sample preparation & analysis

Blood samples were taken from a biobank of patients undergoing cardiac bypass surgery. Ethics approval was given by the South Central NRES committee (Ref: 11/SC/0214) and the University of Southampton ERGO committee (Submission ID:14646). The participant provided written informed consent. All sample and participant data were link anonymised, with the master key kept under secure storage. Samples were acquired from the port of the central venous line. The first 3 mL of blood was discarded before collecting the 6 mL sample into lithium heparin-coated Vacutainer tubes (BD Biosciences, Oxford, UK). Shear-stress was minimized by breaking the Vacutainer seal before sample collection. Samples were centrifuged within one hour twice at 2000 RCF for 10

minutes at room temperature, isolating platelet poor plasma (PPP). The sample was initially stored at -20 °C until transportation to -80°C freezers. The PPP sample was thawed at 37 °C for 10 minutes before 30 µL of PPP was added to 50 µL 0.1 µm double-filtered HEPES buffered saline (dfHBS) with 3 µL of 200 µg mL^{-1} anti-human CD41a IgG1κ BV421 (Cat. 624124, Lot. 4231719, BD Bioscience, Oxford, UK), Samples were incubated for 5 minutes before 10 µL of 83 µg mL^{-1} MFGE8 FITC (Cat. BLAC-FITC, Lot. EE0318-1ML, Cambridge Bioscience, Cambridge, UK) was added and incubated on ice in the dark for a further 10 minutes before analysis using flow cytometry. Following incubation, 1 mL of 0.1 µm dfHBS was added to the incubated sample. Samples were serially diluted to find a concentration that reduced the likelihood of simultaneous detection of two or more particles in the illuminated part of the core stream at once. When an appropriate dilution factor for the sample was determined, the sample was then analysed in a tube containing 1 mL 0.1µm dfHBS and a known number of fluorescent counting beads for enumeration of the sample volume (TruCount Tubes, BD Bioscience, Oxford, UK). An isotype matched control (mouse IgG1κ BV421, Cat. 562438, Lot. 4115857, BD Bioscience, Oxford, UK) was used at the same final concentration as the anti-human CD41a antibody, and analysed at the same dilution as their matched antibody sample. Detailed information on experiment design and acquisition for EVs can be found in **Supplementary Table 2**.

Results

Interdependence of collection angle, diameter, and RI on small particle scattering using Mie theory.

Diameter and composition

In later sections of this work we will discuss how to calibrate commercial flow cytometers using reference beads made of known materials: silica and polystyrene, and with known diameters. We thus start with a brief review of how light is scattered by homogeneous nanospheres and compare this with scattering by extracellular vesicles (EVs), modelled as homogenous spheres covered by a thin membrane of higher refractive index. The discussions are based on Mie theory (see Methods section for more details).

The total scattering cross-section is obtained from the differential cross-section by integration over all solid angles. In the majority of commercial flow cytometers, SSC is collected at 90° to the illumination source. Due to the varying geometries of the collection optics the half-angle (shown as 'ε' in **Figure 1A**) varies. This angle can also vary due to alignment by service engineers and may in part explain the variability that can be seen between the same instruments. This can have a large impact in the comparability between flow cytometers with large differences in collection half-angle due to the non-linear nature of particle scattering. **Figure 2** shows the differential scattering cross-section as a function of the direction of the scattered light (angle ε in **Figure 1A**) for polystyrene and silica beads and EVs of different diameters for illumination at 488 nm wavelength, whose physical properties are given in **Table 2**.

The first thing of note from **Figure 2** are the series of peaks and troughs, known as Mie resonances. There are more Mie resonances in larger particles than smaller particles, this is because they are largely dependent on the ratio of the particle's diameter to the illumination wavelength. Secondly, the position of the Mie resonances is not consistent. It can be seen that particles with the same diameter but different refractive indices have Mie resonances that appear at different angles. Thirdly, the lower the refractive index, the less cumulative light is scattered by the particle and the deeper the Mie resonances tend to be.

These three factors are important for when we consider a flow cytometer's optics which collects the sum of light over a range of angles. Many modern flow cytometry analysers have a SSC collection half-angle (ε) ~50°. In the case of **Figure 2**, it would mean the collected light of each of the particles would be the sum of all angles from 40° to 140°. Jet-in-air sorters however tend to have a collection half-angle of ~30°, meaning the collected light would be the sum of angles from

60° to 120°. If these two collections angles are considered for 250 nm particles in **Figure 2**, it would mean that the deep Mie resonance by the EV composition at 130° would be fully collected by a generic analyser which collects light up to 140° but not by a generic jet-in-air sorter which would collect light up to 120°. The ratio of the EV collected light would therefore be different to that of the silica and polystyrene between the cytometers.

Overall there is no simple relationship between the scattered light intensities in a given direction for different particles since the Mie resonances also shift with the particle refractive index.

Illumination wavelength

While scattered light tends to be collected at 488 nm wavelength in conventional flow cytometers, it is possible to collect at different wavelengths in multi-laser configured flow cytometers, with some new generation flow cytometers choosing to collect light at 405 nm. As an example, we thus show a selection of differential scattering cross-sections for silica spheres at three different wavelengths in **Figure 3** (The effect of wavelength, from 405-640 nm, on polystyrene and silica bead scattering can be seen in the video of **Supplementary Video 1**). While generally similar behaviour to **Figure 2** is found here, we note that the exact details of light scattering, such as absolute values of cross sections and positions of Mie resonances, depend significantly on the illumination wavelength due to the wavelength dependence of refractive indices as well as the differing ratio of light wavelength compared to particle size, as mentioned above.

The data shown in **Figures 2** and **Figure 3** demonstrate that the particle angular scattering distribution varies with both size and composition and, therefore, the diameter of a particle cannot be inferred unless its refractive index and the angle of light collection in the flow cytometer are known.

The illumination beam polarization is also a critical factor when calculating these models, particularly when small collection half-angles are involved, and can lead to large inaccuracies if not accounted for. Since most flow cytometers use linearly polarized illumination beams, all presented models assume linear polarization. Demonstrating the effects of illumination beam polarization on particle light scatter profiles is, however, beyond the scope of this manuscript.

Collection angle

When particles are suspended in a flow stream and passed through a laser beam in a flow cytometer, only a portion of their scattered light is collected. flow cytometers typically collect light in the forward direction and in the sideward direction. Many flow cytometers have a higher sensitivity to small particles using side scatter, rather than forward scatter detection, and side scattering collection (SSC) has therefore mainly been used to gate EVs based on size. This is because side scatter generally allows wider collection angles and because it is well separated from the forward propagating laser beam.

In conventional flow cytometer, SSC is most commonly collected from a cone of half-angle ε at a perpendicular angle to the illuminating laser beam as shown in **Figure 1A** (also shown for) and this is the case in all flow cytometers described in this paper. The maximum range of collection angles of a particle's light scatter is determined by a number of parameters, most notably the flow cell geometry, cuvette geometry, lens numerical aperture and alignment, but may also be affected by the central focusing and diameter of the core stream, the suspending medium refractive index, and the details of the collection optics.

Consequently, the amount of light collected by SSC in a flow cytometer corresponds to the differential scattering cross section (as shown in **Figure 2**) integrated over a certain range of angles around 90°. This integrated cross section as a function of particle composition and size is shown in **Figure 4** for different opening half angles of the collection optics (ε from 0° to 90°) and for two optical geometries: "circular aperture" where light emitted in a cone of the given collection angle is collected, and "square aperture" where light emitted within the collection angle in both the azimuthal and polar angle is collected. When all angles are collected between 0-180°, i.e. for a collection half angle ε = 90°, the integrated scattering cross-section increases continuously with the

particle diameter. As the collection angle decreases, the effect of Mie resonances becomes increasingly significant. For small collection half-angles, it is therefore no longer possible to uniquely determine a particle diameter from the collected light intensity. Both circular and square aperture geometries exhibit very similar behaviour with only very subtle differences (**Supplementary Figure 2**).

Calibration of flow cytometers using FCM$_{PASS}$ software

Based on the discussions above it is therefore clear that in order to derive reliable estimates of EV diameters using conventional flow cytometry one needs to know the collection angle ε of the instrument. One obvious method to obtain the collection angle is by analyzing the imaging optics of the flow cytometer [9]. However, gaining access to proprietary flow cytometer information may not be possible for many laboratories. As an alternative method, we show that the FCM$_{PASS}$ software can obtain a collection half-angle by numerically fitting measured SSC data for known reference particles with simulation results. We performed this analysis for three different flow cytometers: LSR Fortessa, LSR Fortessa X-20, and FACSCanto I.

First, we used analysed polystyrene and silica NIST-traceable beads of different diameters, **Table 1**, to measure their SSC intensities. The median SSC peak height intensities for each bead were inputted into the software. Upon finishing its calculations, the FCM$_{PASS}$ software outputs 4 graphs **Figure 5A-D**. The FCM$_{PASS}$ software first calculates the approximate collection angle by comparing the acquired bead data with every possible collection half-angle from 0-90° in 0.1° increments, **Figure 5A**. The approximated collection angles for each of the cytometers the calibration was performed upon produced results accurate to within 3° (**Table 3**). Upon approximating the collection half-angle, the predicted scattering cross-section of the each of the beads is plotted against the acquired scattering intensity with linear regression then performed, **Figure 5B**. The obtained regression equation allows the conversion of SSC data in arbitrary units to units of scattering cross-section in nm^2. With this information, the software plots a scatter-diameter graph, **Figure 5C**, that allows the diameter vs. intensity relationship to be observed irrespective of refractive index. The final graph is the scatter-refractive index plot, which plots the refractive index vs. intensity relationship irrespective of diameter. **Figure 5C, D** can both be used to interpolate acquired scattering data with modelled scattering data to produce diameter distributions or refractive index distributions.

The manufacturer specified diameter distributions and refractive index distributions of the acquired beads can be seen in **Figure 6A, B**. The acquired data from the beads in **Figure 5** were interpolated with **Figure 5C** to produce the calculated diameter distributions of each bead in **Figure 6C,** and also interpolated with **Figure 5D** to produce the calculated refractive index distributions of each bead in **Figure 6D**. This was repeated for each cytometer with the comparisons summarized in **Figure 7A**,**B**. A more recent demonstration using a CytoFlex was carried out with different sized NIST-Traceable polystyrene and silica beads, **Supplementary Figure 3**.

To perform an interpolation of acquired scattering data to output refractive index distributions, the particles diameter must be known. Acquiring an accurate diameter distribution for extracellular vesicles must be done with an independent measurement of the sample. This measurement can then be correlated with membrane intensity staining as previously demonstrated, assuming the cytometer used is able to resolve the total membrane stained population [19]. To obtain a diameter distribution using interpolation with the scattering data, a refractive index must be assumed. While limited, EV refractive index determination has been demonstrated using NTA or using refractive index data based upon published measurements [12, 13, 14, 15, 16, 17]. It is therefore possible to generate an approximate refractive index using a core-shell model with upper and lower limits. While this is an approximation, current extracellular vesicle refractive index measurements fit within these bounds. Furthermore, provided the results of the interpolation are reported correctly, it is always possible to reproduce or revise the interpolated data when more accurate information becomes available.

With the flow cytometer calibration procedure described above, it is theoretically possible to approximate the diameters of EVs with a known refractive index, as was demonstrated with beads of known refractive index. It should be noted that using this method to approximate the EV diameter distribution should be applied to a population that will not be positive for other particles such as lipoproteins, protein complexes, etc. **Figure 8** demonstrates how diameter distribution can be approximated from scattering data, assuming an average extracellular vesicle refractive index. Platelet poor plasma was stained and gated around anti-CD41 and MFG-E8 staining. The fluorescently positive gated data **Figure 8A** was then interpolated with a scatter-diameter curve such as **Figure 5C**, to produce an approximate EV diameter distribution **Figure 8C**. The resulting diameter distributions fall within each detector bin in a nonlinear manner as a result of the multimodal Mie curves. Thus, the interpolated diameter distribution is a function of several instrument-specific attributes, including collection angles, light scattering geometries, channel binning, and signal processing algorithms. Comparisons of phosphatidylserine staining using MFGE8 to 100 nm fluorescent beads and performance test beads can be seen in **Supplementary Figure 4**. It can be seen that the diameter distribution appears to be bi-modal (**Figure 8C**), with a trough in the range of ~400-480 nm. This trough is an artefact that results from the transposition of the arbitrary light scatter units to diameter (nanometers). This is a direct result of the flow cytometer collection angle and geometry, and can be seen in **Figure 8C** where there is a plateau in the scatter-diameter curve from ~400-480 nm for the predicted EV light scattering using an average EV RI.

To further explain the effect of this type of artefact a dataset was created that had 1 event per detector channel from 200 to 2^{18} (the maximum channel number in the Fortessa X-20), **Supplementary Figure 5**. Interpolating this dataset with the predicted data for the plotted average EV RI curve shows the resulting diameter distribution, where there is again a trough between ~400-480 nm. This artefact further highlights the importance of understanding the flow cytometer collection optics with regard to scattering for its standardization across instruments.

Discussion

This data demonstrates the relationship of particle scattering with composition, diameter, and illumination wavelength. We have also demonstrated that the FCM_{PASS} software is capable of calibrating a flow cytometer's SSC parameter to produce standardized scattering measurements, by using numerical modelling of particle light scattering characteristics combined with reference particles. Importantly, utilizing this technique requires only the acquisition of commercial nanoparticles, with known diameter and refractive index, without the need to acquire proprietary or unknown flow cytometer information. Options are however available for users to specify set collection angles and geometries for modelling. It should be noted that the FCM_{PASS} software, and modelling in general, is most reliable in flow cell-based flow cytometers. Flow cytometers, such as 'jet-in-air' sorters have a user calibrated stream position, with respect to the collection optics, along with having SSC obscuration bars[20]. Extra care with jet-in-air flow cytometer calibration and further calculations must therefore be carried to ensure the accuracy of SSC modelling but it is feasible [21, 22, 23].

Furthermore, the FCM_{PASS} software opens up avenues to allow the conversion of scattering intensity in arbitrary units to either a refractive index measurement or diameter distribution, provided the correct controls are performed. Utilisation of the FCM_{PASS} software in the extracellular vesicle field could therefore be extremely beneficial in standardization of SSC data reporting and also allowing diameter or refractive index measurements between extracellular vesicle sources. While there are limitations in the transposing of arbitrary scattering units to diameters, due to the certain collection angles, as demonstrated within this manuscript, they tend apply to larger vesicles and in highly sensitive systems will account for minority of vesicles, due to the diameter distribution of EVs being a Power law distribution [24].

In order to successfully use this technique in different laboratories, it is important to understand that this technique is reliant on an adequate number of nanoparticle diameters and refractive indices being used, with the reliability of approximated collection angle increasing with a larger

number of bead diameters and compositions analysed. We recommend at least 8 bead diameters are used with at least two compositions to allow for accurate calibration. This methodology for predicting collection angle is currently limited to conventional flow cytometer SSC collection optics, which are collected symmetrically and perpendicular to their illumination. Flow cytometers, such as the Apogee series of instruments, that collect light asymmetrically will still be able to calibrate their measurements using the software, but users will have to input the collection angles manually.

Understanding the implications of EV scattering characteristics has an impact on the interpretation of current EV literature. Firstly, it can clearly be seen that high refractive index materials, such as polystyrene, can only be related to EVs using light scattering if they are calibrated using modelling, e.g. by Mie theory. A method of comparing what a flow cytometer is capable of detecting using light scatter and that does not use modelling would require a well characterised reproducible control that mimics the scatter characteristics of EVs. This type of solution would not provide a way to calibrate axis to standard units or determine the limit of light scatter sensitivity without utilizing light scatter modelling. A need for EV mimetics has been recognised within the field and is under investigation [14, 25]. A method that uses the ratio of forward scatter to side scatter without modelling has been demonstrated to derive particle refractive index, this methodology, however, is limited by the forward scatter sensitivity and will likely never be capable of utilization for the majority of EVs which lie in the 100 nm EV diameter range. This type of methodology is particularly suited to the optics of the Apogee instruments, but may be also be useful for flow cytometers with low collection angles such as jet-in-air sorters where Mie resonances make it impossible, **Figure 4**, to derive the particle diameter >100-150 nm from SSC alone [26]. Secondly, using different wavelengths for scatter collection has benefits and limitations. Shorter wavelengths increase the scattering cross-section of particles, whilst larger wavelengths produce more isotropic scattering characteristics which makes particle sizing easier for the majority of EVs, due to Mie resonances occurring at larger diameters. Implementation of different wavelengths, however, may lead to practical hurdles due to collection lens chromatic aberration, system optical noise, and particle dispersion characteristics. Thirdly, accurate calibration of flow cytometers with reference particles requires access to internal specifications of the flow cytometer, in particular the geometry of the collection optics. In cases where such proprietary component information from the manufacturer is not available, we have demonstrated here a method to determine a sufficiently precise collection angle through numerical fitting of simulated results with measured reference bead data. Finally, upon obtaining a collection half-angle of the instrument we have demonstrated an example of determining the EV diameter distribution in absolute units (nanometers) from flow cytometer data.

By developing further understanding and controls for light scatter detection methods, especially coupled with similar ongoing advances in fluorescence detection, improved standardisation of reported EV data, and therefore reproducibility of studies can be achieved. It is important that these techniques are utilised by the field and that further validation studies which have already shown improvement in standardization and still have areas to improve take place [23]. Ultimately, the development and utilisation of these standardisation techniques will provide a method of reproducing and understanding published data, that is currently lacking, in a field that is rapidly heading towards the development of novel diagnostics, prognostics, theranostics, and therapeutics.

Reference List

1. van der Pol E, Boing AN, Harrison P, et al. Classification, functions, and clinical relevance of extracellular vesicles. Pharmacol Rev. 2012 Jul;64(3):676-705. doi: 10.1124/pr.112.005983. PubMed PMID: 22722893.
2. Chernyshev VS, Rachamadugu R, Tseng YH, et al. Size and shape characterization of hydrated and desiccated exosomes. Anal Bioanal Chem. 2015 May;407(12):3285-301. doi: 10.1007/s00216-015-8535-3. PubMed PMID: 25821114.
3. Yuana Y, Koning RI, Kuil ME, et al. Cryo-electron microscopy of extracellular vesicles in fresh plasma. J Extracell Vesicles. 2013 Dec 31;2. doi: 10.3402/jev.v2i0.21494. PubMed PMID: 24455109; PubMed Central PMCID: PMCPMC3895263.

4. Valkonen S, Pol vE, Böing A, et al. Biological reference materials for extracellular vesicle studies. European Journal of Pharmaceutical Sciences. 2016.
5. Nielsen MH, Beck-Nielsen H, Andersen MN, et al. A flow cytometric method for characterization of circulating cell-derived microparticles in plasma. J Extracell Vesicles. 2014;3. doi: 10.3402/jev.v3.20795. PubMed PMID: 24511371; PubMed Central PMCID: PMCPMC3916676.
6. Rousseau M, Belleannee C, Duchez AC, et al. Detection and quantification of microparticles from different cellular lineages using flow cytometry. Evaluation of the impact of secreted phospholipase A2 on microparticle assessment. PLoS One. 2015;10(1):e0116812. doi: 10.1371/journal.pone.0116812. PubMed PMID: 25587983; PubMed Central PMCID: PMCPMC4294685.
7. Robert S, Poncelet P, Lacroix R, et al. Standardization of platelet-derived microparticle counting using calibrated beads and a Cytomics FC500 routine flow cytometer: a first step towards multicenter studies? J Thromb Haemost. 2009 Jan;7(1):190-7. doi: 10.1111/j.1538-7836.2008.03200.x. PubMed PMID: 18983485.
8. Jayachandran M, Litwiller RD, Owen WG, et al. Characterization of blood borne microparticles as markers of premature coronary calcification in newly menopausal women. Am J Physiol Heart Circ Physiol. 2008 Sep;295(3):H931-H938. doi: 10.1152/ajpheart.00193.2008. PubMed PMID: 18621859; PubMed Central PMCID: PMCPMC2544500.
9. van der Pol E, van Gemert MJ, Sturk A, et al. Single vs. swarm detection of microparticles and exosomes by flow cytometry. J Thromb Haemost. 2012 May;10(5):919-30. doi: 10.1111/j.1538-7836.2012.04683.x. PubMed PMID: 22394434.
10. Mie G. Beiträge zur Optik trüber Medien, speziell kolloidaler Metallösungen. Annalen der Physik. 1908;330(3):377-445. doi: 10.1002/andp.19083300302.
11. C. M. MATLAB functions for Mie scattering and absorption. 2002-11.
12. Beuthan J, Minet O, Helfmann J, et al. The spatial variation of the refractive index in biological cells. Phys Med Biol. 1996 Mar;41(3):369-82. PubMed PMID: 8778819.
13. Gardiner C, Shaw M, Hole P, et al. Measurement of refractive index by nanoparticle tracking analysis reveals heterogeneity in extracellular vesicles. J Extracell Vesicles. 2014;3:25361. doi: 10.3402/jev.v3.25361. PubMed PMID: 25425324; PubMed Central PMCID: PMCPMC4247498.
14. Valkonen S, van der Pol E, Boing A, et al. Biological reference materials for extracellular vesicle studies. Eur J Pharm Sci. 2016 Sep 10. doi: 10.1016/j.ejps.2016.09.008. PubMed PMID: 27622921.
15. van der Pol E, Coumans FA, Sturk A, et al. Refractive index determination of nanoparticles in suspension using nanoparticle tracking analysis. Nano Lett. 2014 Nov 12;14(11):6195-201. doi: 10.1021/nl503371p. PubMed PMID: 25256919.
16. van Manen HJ, Verkuijlen P, Wittendorp P, et al. Refractive index sensing of green fluorescent proteins in living cells using fluorescence lifetime imaging microscopy. Biophys J. 2008 Apr 15;94(8):L67-9. doi: 10.1529/biophysj.107.127837. PubMed PMID: 18223002; PubMed Central PMCID: PMCPMC2275685.
17. Foladori P, Quaranta A, Ziglio G. Use of silica microspheres having refractive index similar to bacteria for conversion of flow cytometric forward light scatter into biovolume. Water Res. 2008 Aug;42(14):3757-66. doi: 10.1016/j.watres.2008.06.026. PubMed PMID: 18662824.
18. Polyanskiy MN. Refractive index database. Available from: https://refractiveindex.info
19. Stoner SA, Duggan E, Condello D, et al. High sensitivity flow cytometry of membrane vesicles. Cytometry Part A : the journal of the International Society for Analytical Cytology. 2016;89(2):196-206. doi: 10.1002/cyto.a.22787.
20. van der Vlist EJ, Nolte-'t Hoen EN, Stoorvogel W, et al. Fluorescent labeling of nano-sized vesicles released by cells and subsequent quantitative and qualitative analysis by high-resolution flow cytometry. Nature protocols. 2012 Jun 14;7(7):1311-26. doi: 10.1038/nprot.2012.065. PubMed PMID: 22722367; eng.
21. Wiklander OPB, Bostancioglu RB, Welsh JA, et al. Systematic Methodological Evaluation of a Multiplex Bead-Based Flow Cytometry Assay for Detection of Extracellular Vesicle Surface Signatures. Frontiers in immunology. 2018 JUN 13 2018;9. doi: 10.3389/fimmu.2018.01326. PubMed PMID: WOS:000435105500001.

22. Morales-Kastresana A, Musich TA, Welsh JA, et al. High Fidelity Detection and Sorting of Nanoscale Vesicles in Viral Disease and Cancer. Journal of Extracellular Vesicles. 2019.
23. van der Pol E, Sturk A, van Leeuwen T, et al. Standardization of extracellular vesicle measurements by flow cytometry through vesicle diameter approximation. J Thromb Haemost. 2018 Mar 25. doi: 10.1111/jth.14009. PubMed PMID: 29575716.
24. van der Pol E, Coumans FA, Grootemaat AE, et al. Particle size distribution of exosomes and microvesicles determined by transmission electron microscopy, flow cytometry, nanoparticle tracking analysis, and resistive pulse sensing. J Thromb Haemost. 2014 Jul;12(7):1182-92. doi: 10.1111/jth.12602. PubMed PMID: 24818656.
25. Varga Z, van der Pol E, Palmai M, et al. Hollow organosilica beads as reference particles for optical detection of extracellular vesicles. J Thromb Haemost. 2018 Jun 7. doi: 10.1111/jth.14193. PubMed PMID: 29877049.
26. van der Pol E, de Rond L, Coumans FAW, et al. Absolute sizing and label-free identification of extracellular vesicles by flow cytometry. Nanomedicine. 2018 Apr;14(3):801-810. doi: 10.1016/j.nano.2017.12.012. PubMed PMID: 29307842.

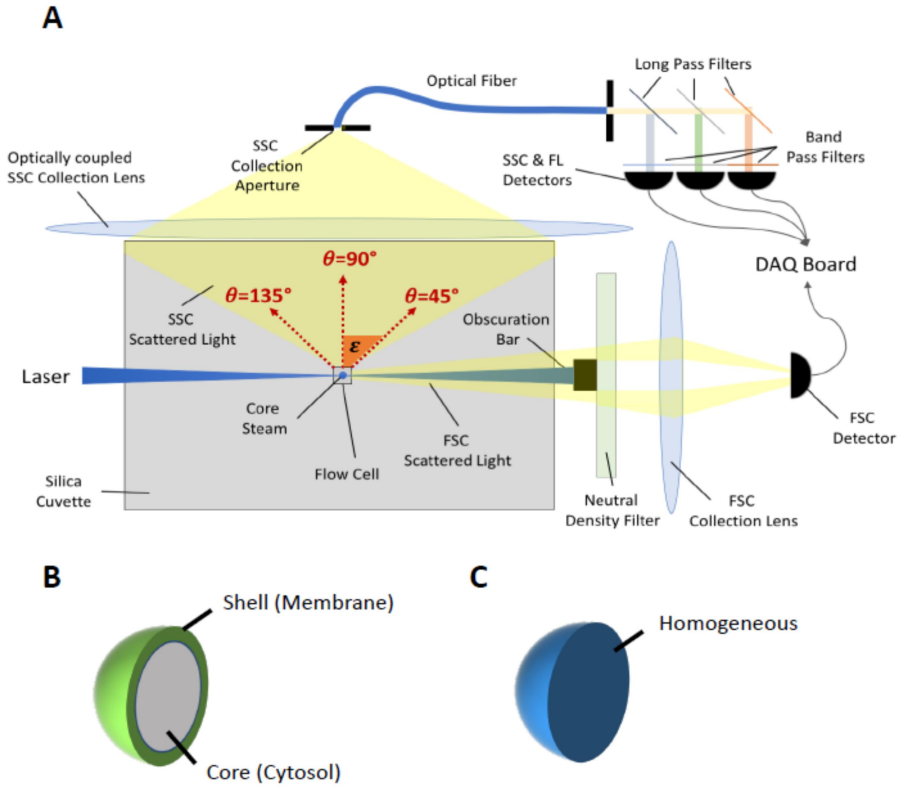

Figure 1. Top view schematic of a flow cytometer with optical fibre and particle composition. A) Particles confined in the core stream (propagating out of the image plane) scatter light from the laser; the direction of scattered light is given by the angle q. The side scattering collection optics collects the scattered light within the collection half-angle ε symmetrically at directions perpendicular to the laser propagation direction, i.e. light is collected from scattering directions q between 90°-ε and 90°+ε. It can be seen that in this case the outer flow cell is the limiting collection angle, which is common. However, any component in the path between the illuminated particle and the light received by the detector can alter the collection angle and geometry of the system. **B)** Core-shell structure representing how an extracellular vesicle would be modelled. The shell representing the phospholipid bilayer, typically 10 nm, and the core representing the cytosolic portion. **C)** Homogeneous sphere representing how silica and polystyrene beads are modelled.

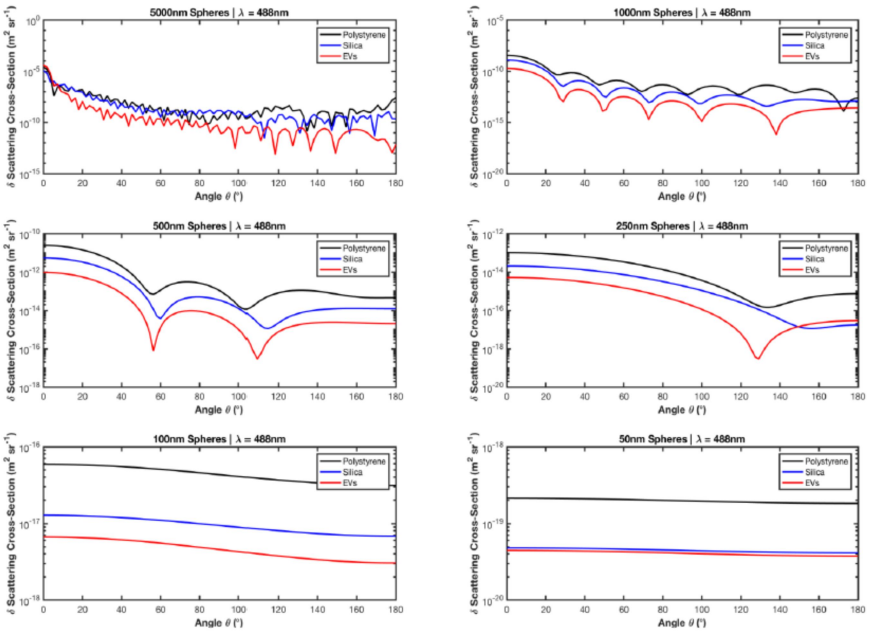

Figure 2. **Effect of diameter and composition on angular scattering distribution.** Angle-dependence of light scattering differential cross section for micro-particles of different composition and different diameters calculated by Mie scattering theory for illumination at 488 nm wavelength. Polystyrene and silica beads are modelled as homogeneous spheres, vesicles as spheres with different refractive indices for the cytosol and for a 10 nm thick membrane.

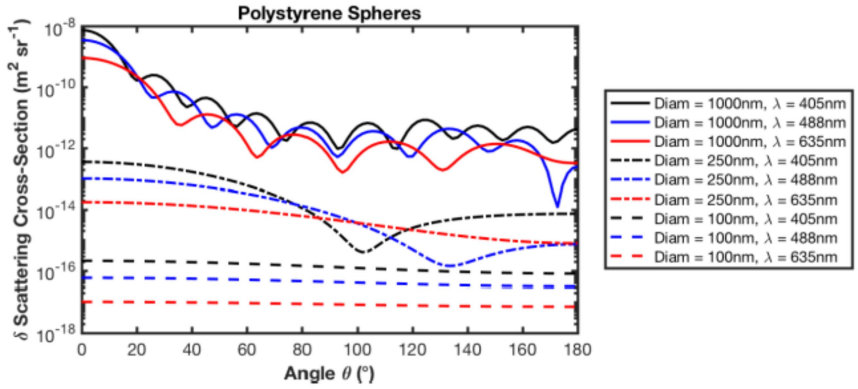

Figure 3. **Effect of wavelength of angular scattering distribution.** Angle-dependence of light scattering differential cross section for silica beads of different diameters at different illumination wavelengths calculated by Mie scattering theory. Bead diameters are 5000 nm (solid lines), 500 nm (dashed), 100 nm (dotted) and light wavelengths are 405 nm (blue lines), 488 nm (green), 633 nm (red).

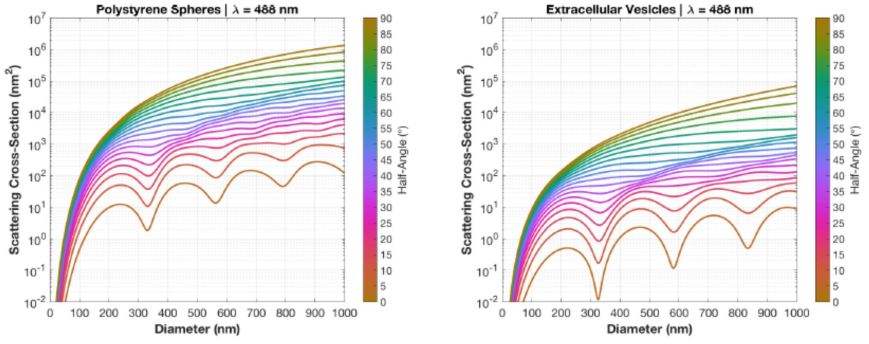

Figure 4. **Effect of collection angle on scatter-diameter curves.** Scattering cross sections integrated over finite collection half angles ε from 5° to 90° in 5° increments with circular apertures for polystyrene spheres (left) and extracellular vesicles (right) versus particle diameter, obtained from integration of the data in Fig. 1 over the corresponding solid angles.

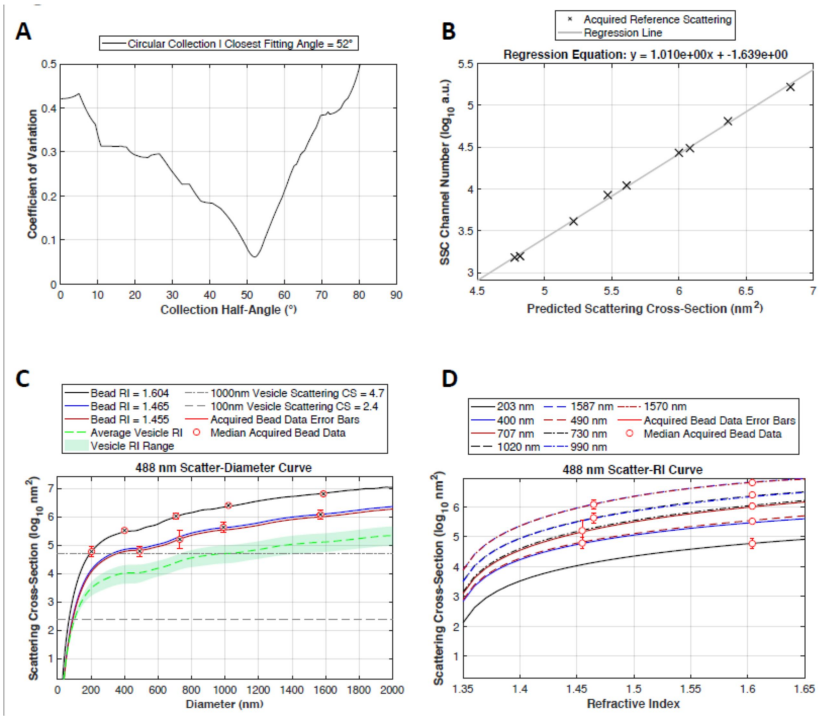

Figure 5. FCM_{PASS} output figures from Fortessa X-20 analysis. (**A**) shows the coefficient of variation (CV) between predicted vs. acquired scattering data from NIST-traceable beads. The collection half-angle with the lowest CV is deemed collection half-angle for the instrument. (**B**) shows a linear regression of predicted vs. acquired data for each bead, with the regression equation providing a means to convert arbitrary scattering data to known units of scattering cross-section in nm^2. (**C**) shows the median SSC-H versus diameter of each bead overlaid with the predicted scattering data for each NIST-traceable bead composition. (**D**) shows the median SSC-H versus refractive index of each NIST-traceable bead overlaid with the predicted scattering data for each bead composition.

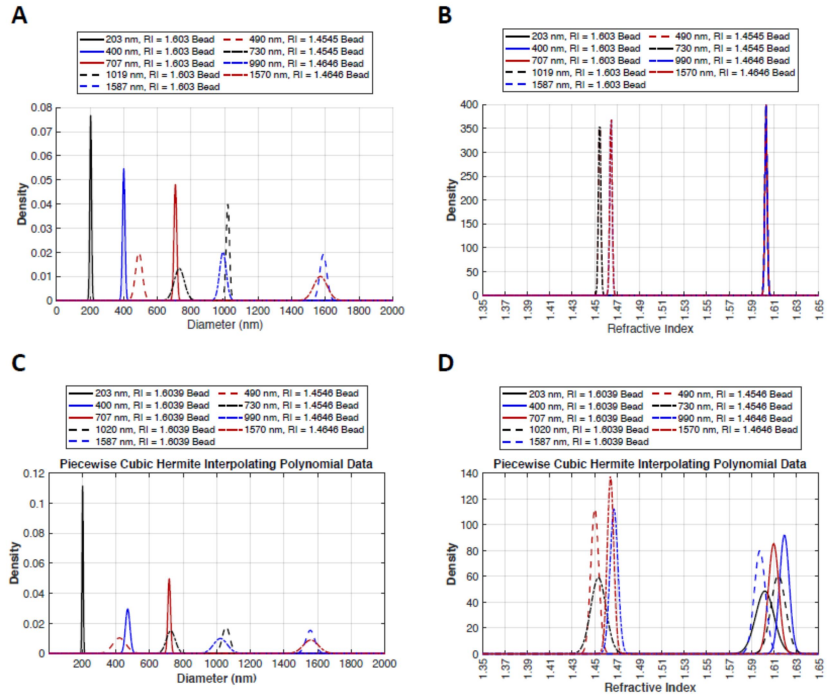

Figure 6. FCM_{PASS} NIST-traceable bead interpolation from Fortessa X-20 analysis. (**A**) shows the expected mean bead diameter and coefficient of variation (CV) of each NIST-traceable bead, based on manufacturer specifications. (**B**) shows the expected refractive index and coefficient of variation (CV) of each NIST-traceable bead, based on manufacturer specifications. (**C**) shows the obtained mean bead diameter and coefficient of variation (CV) of each NIST-traceable bead, based on piecewise cubic hermite polynomial interpolation with modelled data. (**D**) shows the obtained mean bead RI and coefficient of variation (CV) of each NIST-traceable bead, based on piecewise cubic hermite polynomial interpolation with modelled data.

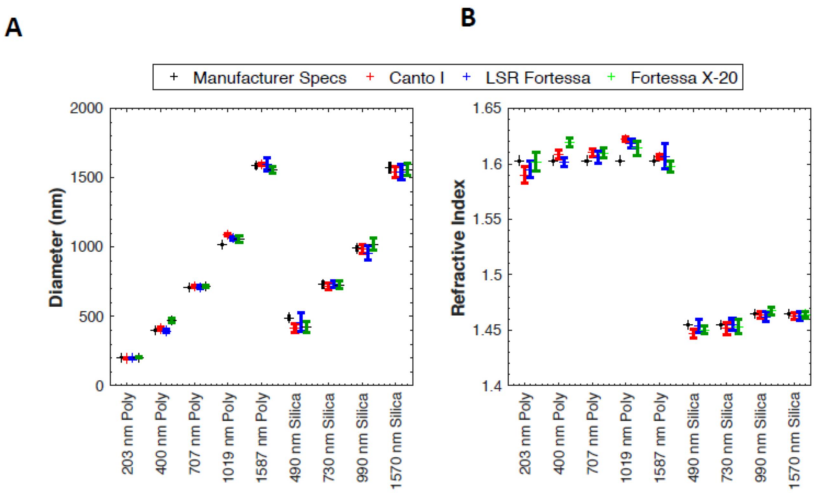

Figure 7. FCM_{PASS} NIST-traceable bead interpolation cytometer comparison. (**A**) shows a comparison between expected (black) mean bead diameter and standard deviation (SD) of each NIST-traceable bead based on manufacturers specifications, and obtained mean bead diameter and SD from three different cytometers based on piecewise cubic hermite polynomial interpolation with modelled data. (**B**) shows a comparison between expected (black) mean refractive index and SD of each NIST-traceable bead based on manufacturers specifications, and obtained mean refractive index and SD from three different cytometers based on piecewise cubic hermite polynomial interpolation with modelled data.

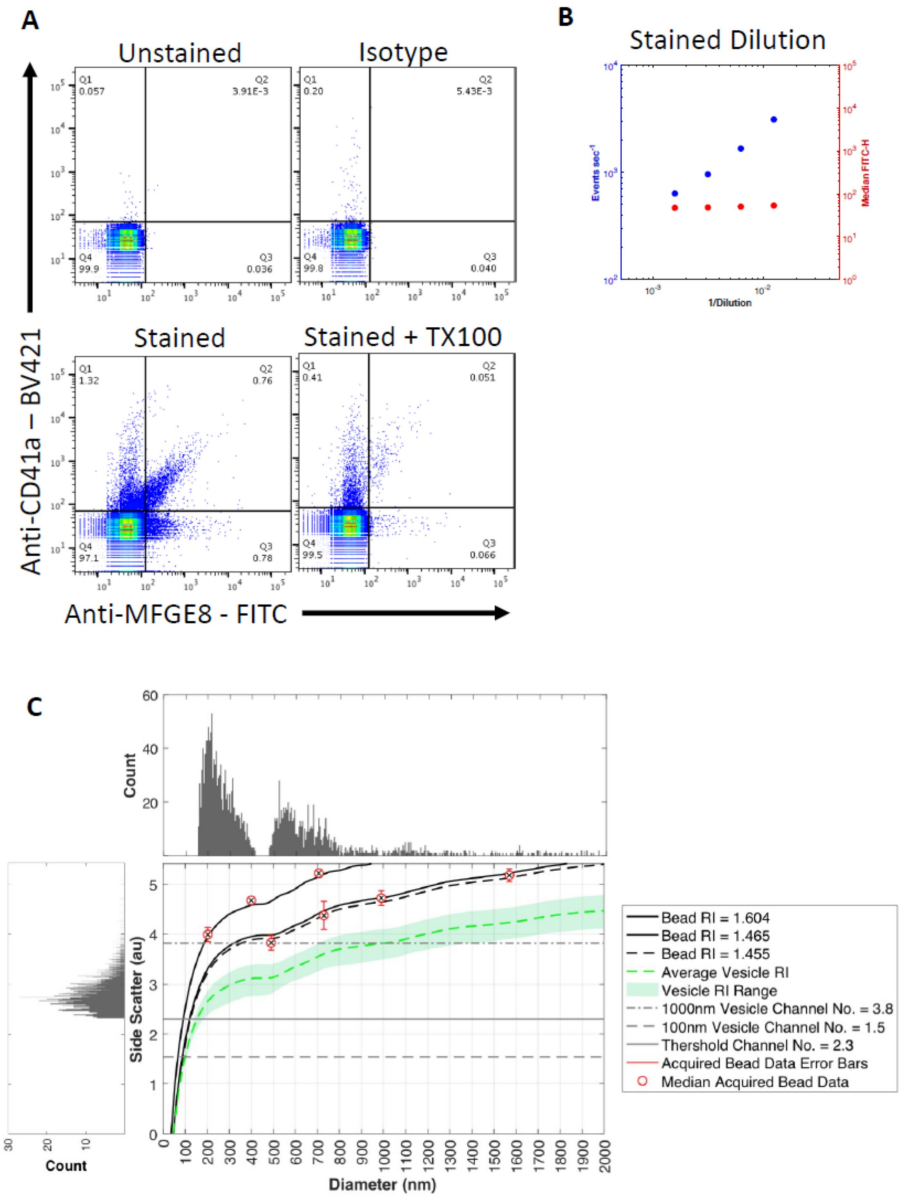

Figure 8. Analysed platelet EVs. (**A**) shows a dot plots for unstained, isotype, stained, and stained + triton X-100 EV populations. (**B**) shows dilution controls of EVs, (**C**) shows the CD41a+ MFGE8+ EVs SSC histogram (left) plotted against the Fortessa X-20 scatter-diameter curve, used to interpolated the SSC data with the average EV RI plotted line to create a diameter distribution (top).

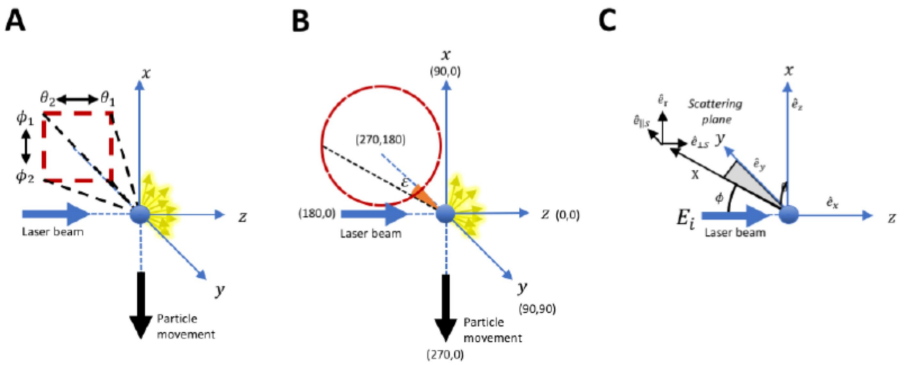

Supplementary Figure 1 shows how θ and ϕ relate to the modelled collection of light in the FCMPASS software with square (**A**) and circular (**B**) geometries. Co-ordinates are shown (θ, ϕ) in degrees, as these are the inputs used within the FCM_{PASS} GUI. For the scattering calculations, these are however first converted to radians automatically in the software. Also shown is the co-ordinate system of the circular geometry annotated by the symbols explained throughout the supplementary methods (**C**), which has been adapted from Bohren and Huffman.

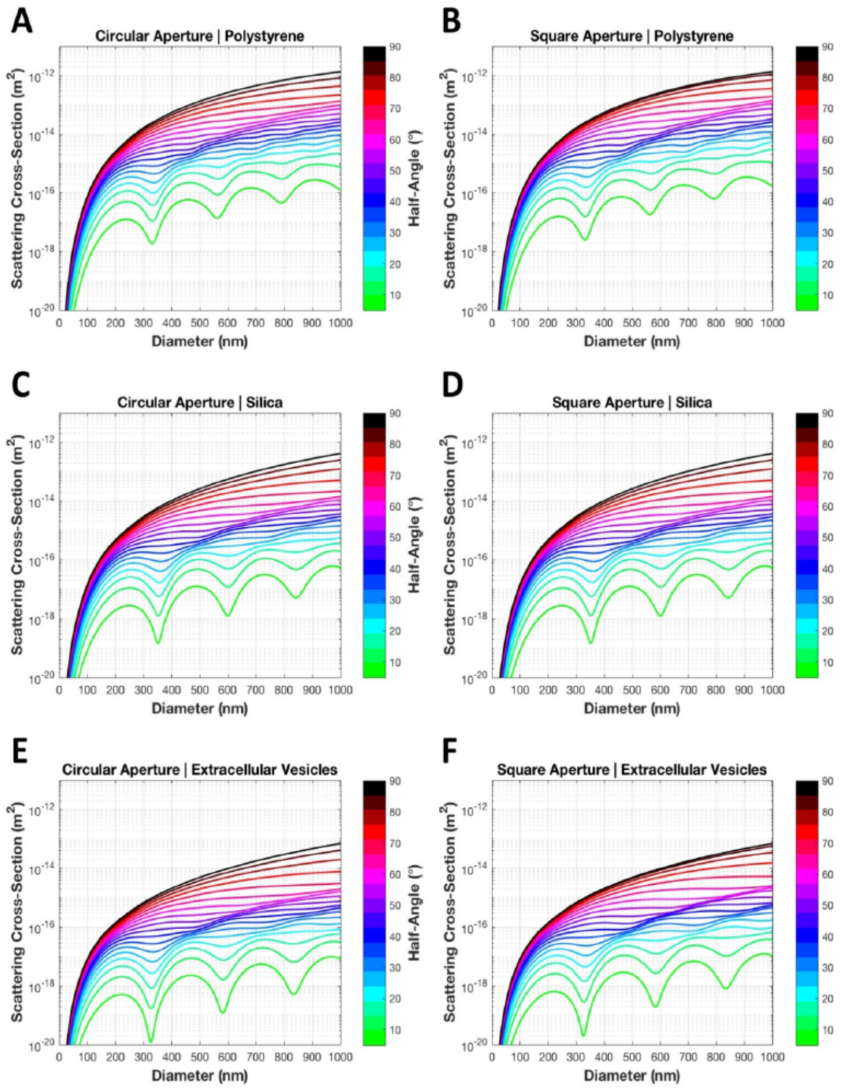

Supplementary Figure 2. Comparison of circular and square collection apertures with varying collection half-angles for polystyrene, silica, and extracellular vesicles.

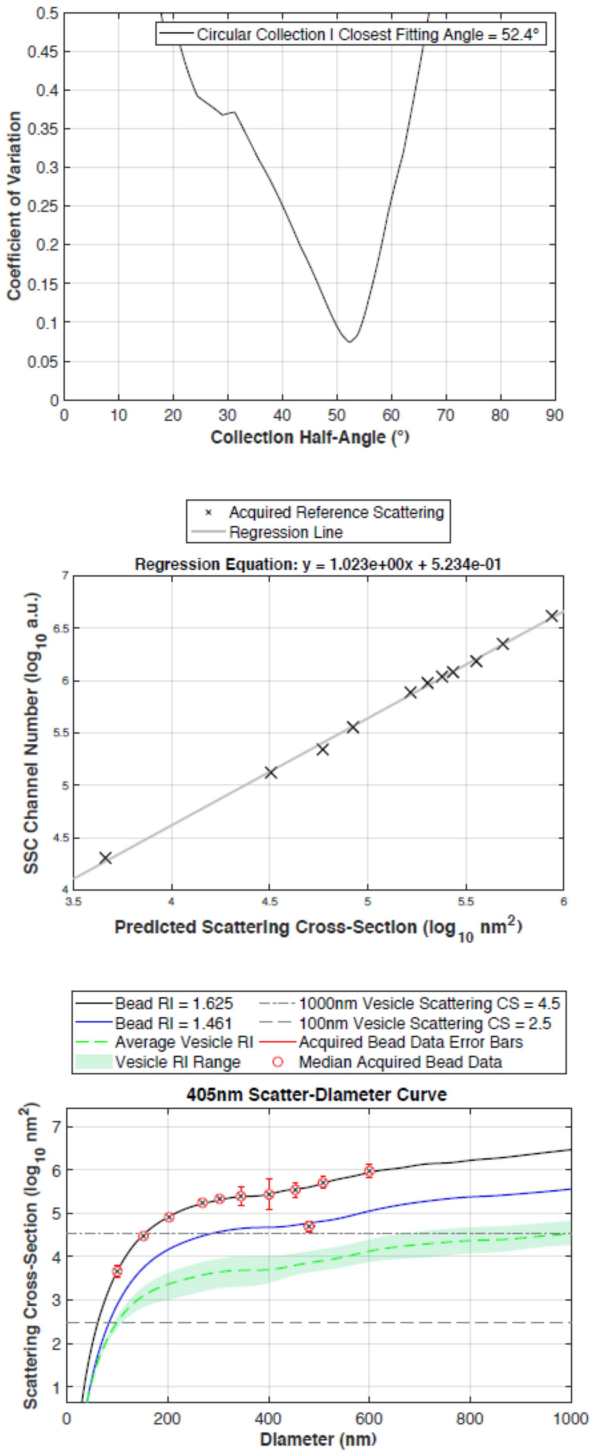

Supplementary Figure 3. Comparison of Phosphatidylserine$^+$ CD41a$^+$ EVs, 100 nm Megamix Plus FSC beads, BD performance test beads. (**A**) shows BD CS&T beads (top), 100 nm Megamix Plus FSC bead (middle) and CD41a+ MFGE8+ EVs (bottom) on fluorescence, (**B**) shows BD CS&T beads (top), 100 nm Megamix Plus FSC bead (middle) and CD41a+ MFGE8+ EVs (bottom) on SSC-H,

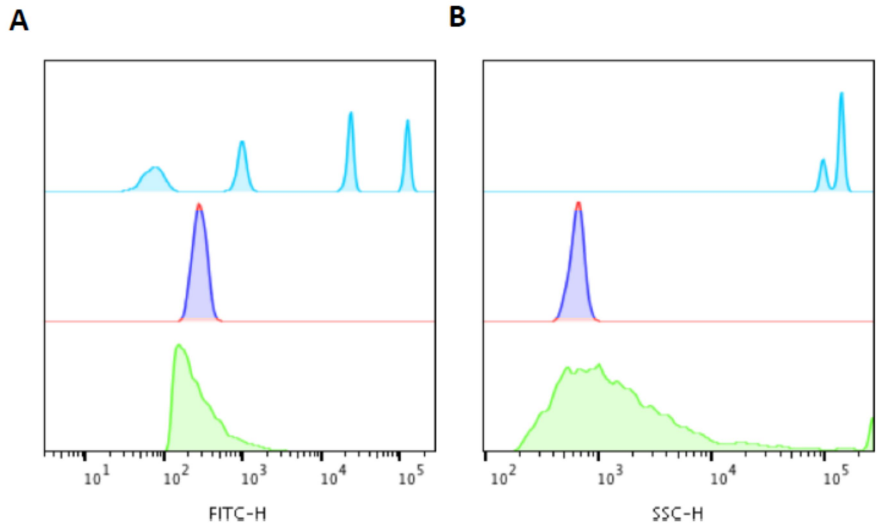

Supplementary Figure 4. Artificial dataset interpolation with predicted average EV RI scattering curve. The top diameter shows a histogram (left) with an artificial dataset containing 1 event per detector channel from 200-2[18]. This artificial SSC data was interpolated with the average EV RI curve on the scatter-diameter plot to create a diameter distribution (top). The area where the predicted average EV RI scattering curve plateaus is highlight in red. The bottom figure shows CD41a+ MFGE8+ EVs SSC data as a histogram (left) plotted against the Fortessa X-20 scatter-diameter curve, used to interpolate the SSC data with the average EV RI plotted line to create a diameter distribution (top).

Composition	Diameter (nm±SD)	Refractive Index (at 589 nm)
Polystyrene	203±5	1.59
	400±7	1.59
	707±8	1.59
	1019±10	1.59
	1587±21	1.59
Silica	490±20	1.45
	730±30	1.45
	990±20	1.46
	1570±40	1.46

Table 1. **Manufacturer specifications of the NIST bead diameters used in the experiment and for modelling.**

Material	Refractive index at wavelength		
	405 nm	488 nm	633 nm
Water	1.345	1.337	1.334
Polystyrene	1.624	1.604	1.586
Silica	1.470	1.463	1.457
EV Membrane	NA	1.480	NA
EV Cytosol	NA	1.380	NA

Table 2. **Refractive indices of materials used within flow cytometer modelling.**

	Collection Half-Angle (°)		
	Geometric Angle	**Fitted Angle**	**Difference**
LSR Fortessa X-20	52	52.05	0.05
LSR Fortessa	52	49.65	2.35
FACS Canto I	52	54.60	2.60

Table 3. Collection angle for side scattered light for several commercial flow cytometers. The "geometric angle" is obtained from the actual geometry of the imaging optics in the instruments, the "fitted angle" is the one obtained by fitting measured scattered intensities of test particles with our numerical model.

Item No.	Item	**Version 1 (S'ton)**	**Version 2 (NCI)**
1	Maetzler core	**Yes**	**Yes**
2	Horak circle integral scripts	**Yes**	**No**
3	Horak square integral scripts	**Yes**	**No**
4	Approximate collection half-angle	**Yes**	**Yes**
5	>10 bead input	**No**	**Yes**
6	Database integration	**No**	**Yes**
7	fcs file integration	**No**	**Yes**
8	Diameter determination from fcs	**No**	**Yes**
9	RI determination from fcs	**No**	**Yes**
10	SSC to scatter-cross section conversion	**No**	**Yes**
11	Write parameters to fcs	**No**	**Yes**
12	scatter-diameter plot output	**Yes**	**Yes**
13	refractive index-diameter plot output	**No**	**Yes**
14	Predicted vs. Acquired scatter regression output	**No**	**Yes**

Supplementary Table 1. FCM_{PASS} Software development comparison of version 1 to version 2.

Framework Information	Description	Reported in Experiment
1. Sample Preparation		
1.1 Purification Method	Sample collection, including any enrichment or isolation procedures	Plasma samples were collected in Lithium-Heparin tubes and centrifuged
1.2 Sample Processing	Sample washing, staining, dilution	Samples were stained with MFG-E8-FITC and CD41a-BV421. Cat. & Lot numbers in M&M.
1.3 Orthogonal sample metrics	Orthoganol EV characterization steps. EV diameter distribution, concentration, etc	NTA and RPS were not a resource available in the laboratory and would be inadequate as a metric for unpurified EVs from plasma.
2. Controls		
2.1 Buffer alone	Buffer only to show background	Shown
2.2 Buffer with reagents	Buffer and reagents only to show background changes compared to buffer only	Not carried out.
2.3 Unstained and isotype controls	Unstained and isotype controls to show background of EV population and non-specific binding	Unstained and matched isotype controls were measured at the same dilution as the stained sample
2.4 Serial dilution	Two-fold serial dilutions (4 minimum) to show dependence of event count, but not intensity, on sample concentration	Serial dilution was carried out on stained samples. The stained sample at an appriopriate event rate for single EV analysis was used for matched stained, isotype, unstained, and detergent treated controls.
2.5 Detergent treated EV samples	Stained sample plus detergent to show lability of population	Samples were treated with 5% Triton X100 for 5 minutes before reanalysis
3. Data Acquisition		
3.1 Trigger channels and thresholds	Channel used for event detection and threshold setting and rationale	A SSC trigger was used on all recordings. This was set arbitrarily by setting threshold to lowest value (200). Voltages were then set based on the event rate (keeping below 1000 events/s for PBS alone), ensuring system optoelectronic noise was off-scale, and ensuring 100 nm Megamix Plus FSC beads were on scale. NIST-traceable beads alone had a SSC threshold set arbitrarily to a threshold at least 1 log decard below the population of beads being detected. Details of thresholds and channel settings can be seen on files uploaded to FlowReposity
3.2 Flow Rate/Volumetric quantification	Sample volumetric flow rate and time of acquisition	A low flow rate was used for all samples with TruCount beads.
3.3 Fluorescence calibration	Use of MESF/ERF/ABC beads to convert intesity values to standard units	MESF controls were not available in the laboratory. BD CS&T beads and Megamix FSC beads were run as controls at the same fluorescence voltages used for each channel
3.4 Scatter calibration	Use of modelling and reference particles to convert intesity values to standard units	Scatter was calibrated using ThermoFisher NIST traceable beads (polystyrene and silica) along with Mie modelling.
4. Data reporting		
4.1 EV number/concentration	Reporting of EV count/concentration of a population with a defined threshold/gate of standard units	The data shown is of single particles demonstrated by serial dilution. The measurement of concentration is not reported as it is not of relevance to the manuscript.
4.2 EV brightness	Displaying/Reporting of EV data in standard units of fluorescence or scatter	MESF beads were not owned at the time of sample acquisition. Comparisons can be made to the BD CS&T beads (Lot 61179) and Megamix Plus FSC beads that were acquired at the same settings as the plasma sampleswhich
4.3 EV diameter	Calculation of EV diameter using fluorescence or scatter measurements with controls	EV diameter is demonstrated by using flow cytometer modelling and interpolating SSC data with predicted data assuming an average EV refractive index (cytosol - 1.38, membrane 1.48). The SSC data interpolated is of CD41a positive and MFGE8 positive staining only (platelet EVs).
4.4 Gating strategy	Rationale for identification of EV-associated events, threshold for populations	**Dilution Control:** All events were gated on 30 seconds of time to normalise acquired event count. **Staining:** A boolean gate was created around TruCount Beads based on FITC-A, FSC-W gating. EVs were then gated on, TruCount negative, anti-CD41a vs anti-MFGE8 staining using quandrant gate based on unstained autofluorescence
5. Data to FlowRepository	Links and brief description of each experiment in FlowRepository	Canto Beads: https://flowrepository.org/id/RvFrYOwODyCAK4F6hsAJ3wLfTzg6f8W0ag1E65xaU1uFuIzCr39Dz4RZxxVYy2yi. LSRFortessa Beads: Fortessa X-20 Beads: https://flowrepository.org/id/RvFrSxnAIz1IaF4qvRw5sE0veUXO8i1Z2ipmc1oKRzQxMG6XE98sayS26MFC3ehH Fortessa X-20 EVs: https://flowrepository.org/id/RvFrKYpyz7gIkJscmWRbGT8HKQzfz3CE0e7e5U0BPsLjW63HuQYcQNrduswHIjbN

Supplementary Table 2. MIFlowCyt-EV experimental considerations.

Supplementary Video 1. Effect of illumination wavelength on angular scattering distributions of spheres. Polystyrene (left) and silica (right). 1000 nm (red), 500 nm (black), 250 nm (blue), and 100 nm (green) spheres angular scattering distributions were modelled at illumination wavelength of 405-640 nm in 1 nm increments.

Supplementary Video 2. Effect of collection half-angle on scatter-diameter relationship of spheres. Angular scattering distribution (top) of polystyrene (top left) and silica (top right) with collection half-angle overlaid. 1000 nm (red), 500 nm (black), 250 nm (blue), and 100 nm (green) spheres. Scatter-diameter curves of polystyrene (bottom left) and silica (bottom right) spheres with the collection half-angle denoted by top plot.

Supplementary Video 3. Effect of illumination wavelength on scatter-diameter relationship of spheres. Scatter-diameter curves of polystyrene (left) and silica (right) spheres at varying collection half-angles with an increasing illumination wavelength from 405-640 nm.